

On trajectories of complex-valued interior transmission eigenvalues

Lukas Pieronek¹ and Andreas Kleefeld^{2,3}

¹ Karlsruhe Institute of Technology, Institute for Applied and Numerical Mathematics, Englerstr. 2, 76131 Karlsruhe, Germany

² Forschungszentrum Jülich GmbH, Jülich Supercomputing Centre, Wilhelm-Johnen-Str., 52425 Jülich, Germany

³ University of Applied Sciences Aachen, Faculty of Medical Engineering and Technomathematics, Heinrich-Mußmann-Str. 1, 52428 Jülich, Germany

E-mail: 1.pieronek@fz-juelich.de and a.kleefeld@fz-juelich.de

May 2022

Abstract. This paper investigates properties of complex-valued eigenvalue trajectories for the interior transmission problem parametrized by the index of refraction for homogeneous media. Our theoretical analysis for the unit disk shows that the only intersection points with the real axis, as well as the unique trajectorial limit points as the refractive index tends to infinity, are Dirichlet eigenvalues of the Laplacian. Complementing numerical experiments even give rise to an underlying one-to-one correspondence between Dirichlet eigenvalues of the Laplacian and complex-valued interior transmission eigenvalue trajectories. We also examine other scatterers than the disk for which similar numerical observations can be made. We summarize our results in a conjecture for general simply-connected scatterers.

Keywords: interior transmission problem, eigenvalue trajectories, complex-valued eigenvalues

1. Introduction

While interior Dirichlet eigenvalues of the Laplacian (IDEs) are among the most famous and long-understood eigenvalues in PDE history, the first appearance of interior transmission eigenvalues (ITEs) reaches back to 1986, cf. [17], when Kirsch studied denseness properties of the far field operator in the context of inverse scattering problems. Accordingly, ITEs correspond to critical and scatterer-specific wave numbers for which the feasibility of many shape-reconstructing sampling methods cannot be ensured. Apart from its physical origins, the related eigenproblem (1) – the interior transmission problem – has also attracted own interest from a functional analytical perspective due to its non-linear and non-selfadjoint nature. ITEs therefore require, in comparison with IDEs that are classified by a self-adjoint and linear operator, quite a

non-standard approach of mathematical investigation which is why they also exhibit surprising structural phenomena. One of those will be the focus of this article and addresses a conjectured link between non-real ITEs and IDEs of the same scattering object.

The importance of such a connection arises from the fact that only little is known about complex-valued ITEs in general. One of the very first results in this direction was the evidence of discreteness of the ITE spectrum for arbitrary scatterers D having infinity as the only accumulation point, see [24, 8]. Further, it is known that for smooth scatterers and smooth indexes of refraction n such that $n > c > 1$ all ITEs are located in a horizontal strip around the real axis, see [25], and there is an ITE-free lemniscate region centered at zero, see [6]. For the special case of a disk in 2D or a ball in 3D as scatterer, existence of non-real ITEs was proven for spherically-stratified media in [21], providing also a more detailed distribution analysis of ITEs, see [10], and first results for the inverse spectral problem, see [9]. In particular, existence of non-real ITEs for arbitrary scatterers D is still an open problem, although existence of infinitely many real-valued ITEs could already be shown in [7], using the intermediate value theorem to find roots of proper misfit functions which then coincide with ITEs by construction. Luckily, there are many numerical algorithms available which indicate the existence of non-real interior transmission eigenvalues for arbitrary scatterers, see for example [12, Table 3], [18, Section 6.10], [11, Tables 4 and 5], [30, Section 5], [32, Section 5], [14, Section 4], [15, Tables 1 and 2], [28, Section 4], [3, Table 5], [16, Tables 1 and 2], [31, Tables 3 and 4], [22, Section 5], [26, Section 5], and [29, Section 5] to mention just a few.

The current paper takes for the first time a dynamic approach to the interior transmission problem and considers trajectories of complex-valued ITEs for homogeneous media which are parametrized by the magnitude of the refractive index n . Restricting to D as a disk first, our main results are that complex-valued ITE trajectories can only intersect the real axis at IDEs as n varies. Conversely, we prove that for any IDE there is $n^* \neq 1$ (in fact infinitely many) and a complex-valued ITE trajectory which intersects that IDE as $n \rightarrow n^*$. Our numerical results even indicate that those trajectories return to the same IDE infinitely many times as $1 < n \rightarrow \infty$ and there are no complex-valued ITE trajectories apart from IDEs. Hence, these findings suggest a one-to-one correspondence between complex-valued ITEs and IDEs as $1 < n \rightarrow \infty$. We can actually prove that those trajectories converge as a whole to the recurrent IDE as $1 < n \rightarrow \infty$. Regarding arbitrary scatterers D , our numerical results further show that complex-valued ITE trajectories now keep away from the real axis for $n > 1$ and thus fail to adopt the recurrent IDE behavior, but they still tend to spiral down towards a unique IDE as $n \rightarrow \infty$, giving again rise to an intrinsic link between complex-valued ITEs and IDEs.

The rest of this paper is organized as follows: after a short introduction to the interior transmission problem, Section 2 presents our theoretical results about complex ITE trajectories for the unit disk. Section 3 provides complementing numerical results

for the unit disk as well as for other scatterers including an ellipse, a deformed ellipse, selected polygons and the unit ball in 3D. We conclude with a conjecture for simply-connected scatterers on the observed relation between complex-valued ITEs and IDEs followed by an outlook of future research in this direction.

2. Theory

The interior transmission problem in the acoustic regime reads

$$\begin{aligned} \Delta w + \kappa^2 n w &= 0 & \text{in } D, \\ \Delta v + \kappa^2 v &= 0 & \text{in } D, \\ v &= w & \text{on } \partial D, \\ \partial_\nu v &= \partial_\nu w & \text{on } \partial D, \end{aligned} \tag{1}$$

and is a system of Helmholtz equations coupled through the boundary data which reflect continuous transmission conditions for time-harmonic waves. Here, D is a simply-connected domain and $n \in L^\infty(D)$ denotes the index of refraction that we assume to be constant and positive throughout this work. We call a wave number $\kappa_n \in \mathbb{C} \setminus \{0\}$ for $n \neq 1$ an ITE if there exist non-trivial $v_n, w_n \in L^2(D)$ such that $(v_n - w_n) \in H_0^2(D)$ which solve (1). In this section we restrict to the unit disk $D \subset \mathbb{R}^2$ so that ITP eigenfunction pairs are spanned by the Fourier Bessel functions

$$\begin{aligned} v_n(r, \varphi) &= J_p(\kappa_n r) \cos(p\varphi), & \left(v_n(r, \varphi) = J_p(\kappa_n r) \sin(p\varphi), p \neq 0 \right), \\ w_n(r, \varphi) &= \alpha_n J_p(\sqrt{n} \kappa_n r) \cos(p\varphi), & \left(w_n(r, \varphi) = \alpha_n J_p(\sqrt{n} \kappa_n r) \sin(p\varphi), p \neq 0 \right), \end{aligned} \tag{2}$$

where $p \in \mathbb{N}_0$, $\alpha_n \in \mathbb{C} \setminus \{0\}$ is a coefficient to match the ITP boundary conditions in (1) and J_p solves

$$x^2 J_p''(x) + x J_p'(x) + (x^2 - p^2) J_p(x) = 0. \tag{3}$$

Hence, we see that ITEs κ_n are equivalently characterized as roots of

$$F_p(\kappa, n) := \kappa \left(J_p'(\kappa) J_p(\kappa \sqrt{n}) - \sqrt{n} J_p(\kappa) J_p'(\kappa \sqrt{n}) \right). \tag{4}$$

To put ourselves into the framework of eigenvalue trajectories, recall from the implicit function theorem that in a local open neighborhood of any n subject to $\partial_\kappa F_p(n, \kappa) \neq 0$ there is a unique continuously-differentiable mapping $n \mapsto \kappa_n$ (which we will also denote by κ_n with derivative κ_n') such that $F_p(n, \kappa) = 0$ if and only if $\kappa = \kappa_n$. For the rest of this paper, a complex-valued ITE trajectory κ_n has to be understood as fulfilling $\kappa_n \notin \mathbb{R}$ for at least one n . We start with a qualitative difference between real- and non-real ITEs.

Lemma 1. *Let κ_n be an ITE for some $n \neq 1$ whose eigenfunction pair (v_n, w_n) is given by (2) for some $p \in \mathbb{N}_0$. Then it holds that*

$$\int_D |v_n|^2 - n |w_n|^2 dx = \begin{cases} \frac{(1-n)}{2} J_p(\kappa_n)^2 \int_0^{2\pi} \cos(p\varphi)^2 d\varphi, & \text{for } \kappa_n \in \mathbb{R}, \\ 0, & \text{else.} \end{cases} \tag{5}$$

Proof. Let (v_n, w_n) be as in (2) with cosine as angular part. If $\kappa_n \notin \mathbb{R}$, it follows by Lemma 5 from [23, p. 43] that

$$\int_D |v_n|^2 - n|w_n|^2 dx = 0 .$$

In the other case, that is $\kappa_n \in \mathbb{R}$, we obtain by using polar coordinates

$$\int_D v_n^2 - n w_n^2 dx = \int_0^{2\pi} \cos(p\varphi)^2 d\varphi \int_0^1 (J_p(\kappa_n r)^2 - n \alpha_n^2 J_p(\sqrt{n} \kappa_n r)^2) r dr .$$

Next, we employ formula (5.14.5) from [20, p. 129] to evaluate

$$\int_0^1 J_p(\kappa_n r)^2 r dr = \frac{1}{2} \left[J_p'(\kappa_n)^2 + \left(1 - \frac{p}{\kappa_n^2}\right) J_p(\kappa_n)^2 \right] \quad (6)$$

and similarly, including the ITP boundary conditions via $\alpha_n^2 > 0$,

$$\begin{aligned} n \int_0^1 \alpha_n^2 J_p(\sqrt{n} \kappa_n r)^2 r dr &= \frac{1}{2} \left[n \alpha_n^2 J_p'(\sqrt{n} \kappa_n)^2 + n \left(1 - \frac{p}{n \kappa_n^2}\right) \alpha_n^2 J_p(\sqrt{n} \kappa_n)^2 \right] \\ &= \frac{1}{2} \left[J_p'(\kappa_n)^2 + \left(n - \frac{p}{\kappa_n^2}\right) J_p(\kappa_n)^2 \right] . \end{aligned} \quad (7)$$

Subtracting (7) from (6) yields

$$\int_D v_n^2 - n w_n^2 dx = \frac{(1-n)}{2} J_p(\kappa_n)^2 \int_0^{2\pi} \cos(p\varphi)^2 d\varphi .$$

This completes the proof if cosine is the angular part of the eigenfunction pair. The case of sine with $p > 0$ follows along the same lines, noting that

$$\int_0^{2\pi} \cos(p\varphi)^2 d\varphi = \int_0^{2\pi} \sin(p\varphi)^2 d\varphi = \pi .$$

□

Lemma 1 yields an immediate conclusion for the intersection points of complex-valued ITE trajectories with the real axis.

Corollary 2. *Let κ_n be a continuous ITE trajectory whose eigenfunction pair (v_n, w_n) is given by (2) for some $p \in \mathbb{N}_0$. Let $n \in (n^* - \epsilon, n^* + \epsilon)$, $\epsilon > 0$ sufficiently small and $n^* \neq 1$. If $\kappa_{n^*} \in \mathbb{R}$, but $\kappa_n \in \mathbb{C} \setminus \mathbb{R}$ for all $n \in (n^* - \epsilon, n^* + \epsilon) \setminus \{n^*\}$, then κ_{n^*} is an IDE with Laplacian eigenfunction v_{n^*} (the same holds true for $\sqrt{n^*} \kappa_{n^*}$ and w_{n^*}).*

Proof. This follows by (5) and continuity of $n \mapsto \int_D |v_n|^2 - n|w_n|^2 dx$. □

Next, we show that complex-valued ITE trajectories κ_n approach IDEs in specific angles. At these points trajectories fail to be differentiable as indicated by the implicit function theorem since they arise in complex-conjugated and thus intersecting pairs. In particular, there is an ambiguity of ingoing and outgoing directions.

Lemma 3. *Let κ_n be a continuous ITE trajectory whose eigenfunction pair (v_n, w_n) is given by (2) for some $p \in \mathbb{N}_0$. Let $n \in (n^* - \epsilon, n^* + \epsilon)$, $\epsilon > 0$ sufficiently small and $n^* \neq 1$. If κ_{n^*} is an IDE such that $J_p(\kappa_{n^*}) = 0$, then it holds that $\lim_{n \rightarrow n^*} |\kappa'_n| = \infty$. Further, $\lim_{n \nearrow n^*} \arg(\kappa'_n) \in \{\pm\pi/3, \pi\}$ and $\lim_{n \searrow n^*} \arg(\kappa'_n) \in \{\pm\pi/3, \pi\}$ for $n^* > 1$ and $\lim_{n \nearrow n^*} \arg(\kappa'_n) \in \{0, \pm 2\pi/3\}$ and $\lim_{n \searrow n^*} \arg(\kappa'_n) \in \{0, \pm 2\pi/3\}$ for $0 < n^* < 1$. In particular, ingoing/outgoing angles at κ_{n^*} which are integer multiples of π correspond to real-valued trajectory parts, respectively.*

Proof. By the implicit function theorem, κ_n is differentiable with

$$\kappa'_n = -\frac{\partial_n F_p(n, \kappa)|_{(n, \kappa_n)}}{\partial_\kappa F_p(n, \kappa)|_{(n, \kappa_n)}}$$

as long as

$$\partial_\kappa F_p(n, \kappa) = (n-1)\kappa J_p(\kappa) J_p(\sqrt{n}\kappa) \quad (8)$$

does not vanish for $\kappa = \kappa_n$. For this to happen, κ_n must be an IDE and in particular real-valued. For the latter representation, we used the Bessel equation (3) to replace arising second order derivatives of J_p . Similarly, incorporating additionally $F_p(n, \kappa_n) = 0$, we obtain

$$\partial_n F_p(n, \kappa)|_{(n, \kappa_n)} = \frac{(n\kappa_n^2 - p^2)}{2n} J_p(\kappa_n) J_p(\sqrt{n}\kappa_n) + \frac{\kappa_n^2}{2\sqrt{n}} J'_p(\kappa_n) J'_p(\sqrt{n}\kappa_n) \quad (9)$$

so that κ'_n becomes, exploiting again the ITP boundary conditions,

$$\begin{aligned} \kappa'_n &= -\frac{(n\kappa_n^2 - p^2)}{2n(n-1)\kappa_n} - \frac{\kappa_n J'_p(\kappa_n) J'_p(\sqrt{n}\kappa_n)}{2\sqrt{n}(n-1)J_p(\kappa)J_p(\sqrt{n}\kappa)} \\ &= -\frac{(n\kappa_n^2 - p^2)}{2n(n-1)\kappa_n} - \frac{\kappa_n J'_p(\kappa_n)^2}{2n(n-1)J_p(\kappa_n)^2}. \end{aligned} \quad (10)$$

In this form, we see that $\lim_{n \nearrow n^*} |\kappa'_n| = \infty$ since $J_p(\kappa_{n^*}) = 0$ while $J'_p(\kappa_{n^*}) \neq 0$ which follows from the classical fact that the roots of J_p and J'_p are distinct.

In order to determine the ingoing/outgoing trajectory directions as $n \rightarrow n^*$ but circumvent the tangential blow-up behavior, we note that $J_p(\kappa) = (\kappa - \kappa_{n^*})h(\kappa)$, where $h(\kappa_{n^*}) = J'_p(\kappa_{n^*}) \neq 0$. We can therefore rewrite (10) in a neighborhood of κ_{n^*} as

$$[(\kappa_n - \kappa_{n^*})^3]' = 3\kappa'_n(\kappa_n - \kappa_{n^*})^2 = -\frac{3(n\kappa_n^2 - p^2)}{2n(n-1)\kappa_n}(\kappa_n - \kappa_{n^*})^2 - \frac{3\kappa_n J'_p(\kappa_n)^2}{2n(n-1)h(\kappa_n)^2}$$

and obtain by integration

$$(\kappa_n - \kappa_{n^*})^3 = -\int_{n^*}^n \frac{3(t\kappa_t^2 - p^2)}{2t(t-1)\kappa_t}(\kappa_t - \kappa_{n^*})^2 + \frac{3\kappa_t J'_p(\kappa_t)^2}{2t(t-1)h(\kappa_t)^2} dt.$$

Since κ_n is continuous by assumption, $n \mapsto (\kappa_n - \kappa_{n^*})^3 \in C^1((n^* - \epsilon, n^* + \epsilon))$, so

$$\lim_{n \rightarrow n^*} -\frac{3\kappa_n J'_p(\kappa_n)^2}{2n(n-1)h(\kappa_n)^2} = -\frac{3\kappa_{n^*}}{2n^*(n^*-1)} \neq 0$$

yields that

$$\lim_{n \rightarrow n^*} 3 \arg \left((\kappa_n - \kappa_{n^*}) / (n - n^*) \right) = \arg \left([(\kappa_n - \kappa_{n^*})^3]'_{|n=n^*} \right) = -\pi$$

for $n^* > 1$ and

$$\lim_{n \rightarrow n^*} 3 \arg \left((\kappa_n - \kappa_{n^*}) / (n - n^*) \right) = \arg \left([(\kappa_n - \kappa_{n^*})^3]'_{|n=n^*} \right) = 0$$

for $0 < n^* < 1$. Comparing with $[(\kappa_n - \kappa_{n^*})^3]' = 3(\kappa_n - \kappa_{n^*})^2 \kappa'_n$, we finally conclude that $\lim_{n \nearrow n^*} \arg(\kappa'_n) \in \{\pm\pi/3, \pi\}$ and $\lim_{n \searrow n^*} \arg(\kappa'_n) \in \{\pm\pi/3, \pi\}$ for $n^* > 1$ and $\lim_{n \nearrow n^*} \arg(\kappa'_n) \in \{0, \pm 2\pi/3\}$ and $\lim_{n \searrow n^*} \arg(\kappa'_n) \in \{0, \pm 2\pi/3\}$ for $0 < n^* < 1$.

It remains to prove that the two angles which are integer multiples of π correspond to real-valued trajectory parts, respectively. This follows, restricting to $n \nearrow n^*$ for the sake of presentation, if we can show that $\Im(\kappa'_n) \geq 0$ for all κ_n sufficiently close to κ_{n^*} such that $\Im(\kappa_n) \geq 0$ and further constrained by $\Re(\kappa_n - \kappa_{n^*}) > |\Im(\kappa_n)|$ in case of $n^* > n > 1$ and $\Re(\kappa_n - \kappa_{n^*}) < -|\Im(\kappa_n)|$ for $0 < n < n^* < 1$. These complex-valued κ_n -regions excluding the real axis are by Corollary 2 indeed locally non-restrictive for approaching κ_{n^*} asymptotically tangential to the real axis, but imply due to $\Im(\kappa'_n) \geq 0$ that $\lim_{n \nearrow n^*} \Im(\kappa_n) \geq 0$ which then contradicts $\lim_{n \rightarrow n^*} \kappa_n \neq \kappa_{n^*} \in \mathbb{R}$. The complementing case $n \searrow n^*$ can then be proven in a similar fashion, showing that ITE trajectories κ_n cannot escape from the real axis tangentially. These results can be seen as generalizations of the fact that poles of order 2 induce locally hyperbolic sectors for *autonomous* holomorphic flows, see [5].

In order to verify that $\Im(\kappa'_n) \geq 0$ for $n < n^*$ sufficiently close and all $\Im(\kappa_n) \geq 0$ subject to the aforementioned constraints, we confine ourselves to $\Im(\kappa_n) > 0$ since ITEs occur in complex conjugated pairs. We define for fixed n the real-meromorphic function

$$d_n(\kappa) := -\frac{(n\kappa^2 - p^2)}{2n(n-1)\kappa} - \frac{g_p(\kappa)}{2n(n-1)(\kappa - \kappa_{n^*})^2}$$

as a replacement for (10) and set

$$g_p(\kappa) := \frac{\kappa J'_p(\kappa)^2}{h(\kappa)^2}.$$

We show in the following that $\arg(d_n(\kappa))$ is dominated by

$$\begin{aligned} & \arg \left(-(n-1)^{-1}(\kappa - \kappa_{n^*})^{-2} \right) \\ &= \begin{cases} \pi - 2 \arg(\kappa - \kappa_{n^*}), & \text{if } n > 1, \Re(\kappa - \kappa_{n^*}) > \Im(\kappa) > 0, \\ -2 \arg(\kappa - \kappa_{n^*}), & \text{if } 0 < n < 1, \Re(\kappa - \kappa_{n^*}) < -\Im(\kappa) < 0 \end{cases} \end{aligned} \quad (11)$$

in a neighborhood of κ_{n^*} which then yields our assertion since $\Im(-(n-1)^{-1}(\kappa - \kappa_{n^*})^{-2}) > 0$ for all κ under consideration. In order to make the argument rigorous, we observe that $g_p(\kappa_{n^*}) = \kappa_{n^*} > 0$, and a straightforward yet lengthy calculation shows that $g'_p(\kappa_{n^*}) = 0$ as well as

$$g''_p(\kappa_{n^*}) = \frac{-8\kappa_{n^*}^2 + 8p^2 + 1}{6\kappa_{n^*}} < 0.$$

The last inequality follows by standard lower bounds on the roots of Bessel functions, see for instance [1, 4]. The second-order approximation of g_p around κ_{n^*} therefore reveals for κ sufficiently close to κ_{n^*} that

$$\Im(g_p(\kappa)) = \begin{cases} \leq 0, & \text{if } \Re(\kappa - \kappa_{n^*}) > \Im(\kappa) > 0, \\ \geq 0, & \text{if } \Re(\kappa - \kappa_{n^*}) < -\Im(\kappa) < 0. \end{cases}$$

In the first case of the right-hand side above we can estimate for $n^* > n > 1$

$$0 < \frac{\pi}{2} - \theta < \arg\left(-\frac{g_p(\kappa)}{2n(n-1)(\kappa - \kappa_{n^*})^2}\right) < \arg\left(- (n-1)^{-1}(\kappa - \kappa_{n^*})^{-2}\right) < \pi, \quad (12)$$

where we employed (11) and, for the lower bound, restrict additionally κ such that $-\theta < \arg(g_p(\kappa)) \leq 0$ for any fixed $0 < \theta < \pi/2$. Note that θ can indeed be chosen arbitrarily small in a neighborhood around κ_{n^*} since $\arg(g_p(\kappa_{n^*})) = 0$. In the other case, that is $\Re(\kappa - \kappa_{n^*}) < -\Im(\kappa) < 0$ and κ sufficiently close to κ_{n^*} correspondingly, we obtain similarly for $0 < n < n^* < 1$

$$0 < \arg\left(- (n-1)^{-1}(\kappa - \kappa_{n^*})^{-2}\right) < \arg\left(-\frac{g_p(\kappa)}{2n(n-1)(\kappa - \kappa_{n^*})^2}\right) < \frac{\pi}{2} + \theta < \pi.$$

In both cases, we see that

$$\Im\left(-\frac{g_p(\kappa)}{2n(n-1)(\kappa - \kappa_{n^*})^2}\right) > 0 \quad (13)$$

and, to verify that $\Im(d_n(\kappa))$ is likewise positive, we are left to show that adding $-(n\kappa^2 - p^2)/(2n(n-1)\kappa)$ to the left-hand side of (13) does not affect the sign. For this we may confine to $\arg(\kappa - \kappa_{n^*})$ close to 0 or π , respectively, since the sign of (13) is in this range most sensitive to additive perturbations thanks to the definition of θ . We first compute for $1 < n < n^*$ and $\Re(\kappa - \kappa_{n^*}) > \Im(\kappa) > 0$

$$\begin{aligned} \pi &< \pi + \arg\left(\frac{(n\kappa^2 - p^2)}{2n(n-1)\kappa}\right) < \pi + \arg(n\kappa^2 - p^2) < \pi + \arg(\kappa^2 - p^2) \\ &< \pi + \arg(\kappa^2 - \kappa_{n^*}^2) = \pi + \arg((\kappa - \kappa_{n^*})(\kappa + \kappa_{n^*})) < \pi + 2\arg(\kappa - \kappa_{n^*}) < \frac{3\pi}{2}. \end{aligned} \quad (14)$$

Here, the first inequality from the bottom line holds since $p < \kappa_{n^*}$ as a root of J_p , see again [1, 4]. Combining (12) and (14), we obtain for $\arg(\kappa - \kappa_{n^*}) > 0$ small that

$$\begin{aligned} \Im(d_n(\kappa)) &> \left|\frac{(n\kappa^2 - p^2)}{2n(n-1)\kappa}\right| \Im\left(e^{i(\pi+2\arg(\kappa-\kappa_{n^*}))}\right) \\ &\quad + \left|\frac{g_p(\kappa)}{2n(n-1)(\kappa - \kappa_{n^*})^2}\right| \Im\left(e^{i(\pi-2\arg(\kappa-\kappa_{n^*}))}\right). \end{aligned}$$

Since the first summand is bounded as $\kappa \rightarrow \kappa_{n^*}$ while the second blows up, we can find a neighborhood of κ_{n^*} such that

$$\Im(d_n(\kappa)) > \left(\left| \frac{g_p(\kappa)}{2n(n-1)(\kappa - \kappa_{n^*})^2} \right| - \left| \frac{(n\kappa^2 - p^2)}{2n(n-1)\kappa} \right| \right) \Im(e^{i(\pi - 2 \arg(\kappa - \kappa_{n^*}))}) > 0$$

which thus yields the assertion in the case $n^* > n > 1$ and κ sufficiently close to κ_{n^*} such that $\Re(\kappa - \kappa_{n^*}) > \Im(\kappa) > 0$. In the other case, that is $\Re(\kappa - \kappa_{n^*}) < -\Im(\kappa) < 0$ and $0 < n < n^* < 1$, we even have

$$\Im\left(-\frac{(n\kappa^2 - p^2)}{2n(n-1)\kappa}\right) > 0 \quad (15)$$

as long as $\Re(n\kappa^2) > p^2$ which is appropriate to assume since $\sqrt{n^*}\kappa_{n^*} > p$ as an IDE according to Corollary 2 and [1, 4] again. In particular, (13) ensures that also $\Im(d_n(\kappa)) > 0$ for $0 < n < n^* < 1$ and κ sufficiently close to κ_{n^*} such that $\Re(\kappa - \kappa_{n^*}) < -\Im(\kappa) < 0$. This finally completes the proof of $\lim_{n \nearrow n^*} \arg(\kappa'_n) \notin \{0, \pi\}$ for ITE trajectories $\kappa_n \rightarrow \kappa_{n^*}$ with non-trivial imaginary part. \square

Remark 4. According to Lemma 5, continuous ITE trajectories κ_n , which are locally real-valued in n , can only escape from the real axis at selected IDEs κ^* . Theorem 5 below then guarantees that locally real-valued ITE trajectories admit natural extensions across κ^* which are globally real-valued. Likewise, one can argue that complex-valued ITE trajectories can be extended to have continuous angles when intersecting the real axis. However, one could also consider continuous ITE trajectories with different incident and outgoing directions at κ^* . As we will see in the numerical section when comparing complex-valued ITE trajectories of an ellipse with major axis 1 and minor axis 0.5 with those of the unit disk, they are indeed only similar to each other if one restricts complex-valued ITE trajectories for the latter to persist in the same half plane as $n \rightarrow \infty$, cf. Figures 1 and 4.

The next theorem shows that the three admissible angles at IDEs κ^* such that $J_p(\kappa^*) = 0$ do even occur simultaneously by three corresponding ITE trajectories. In this way, it also yields an alternative existence proof for non-real ITEs near the IDEs.

Theorem 5. Let κ_n be a continuous and complex-valued ITE trajectory whose eigenfunction pair (v_n, w_n) is given by (2) for some $p \in \mathbb{N}_0$. Let $n \in (n^* - \epsilon, n^* + \epsilon)$, $\epsilon > 0$ sufficiently small and $n^* \neq 1$. If κ_{n^*} is an IDE such that $J_p(\kappa_{n^*}) = 0$, then there exists a further ITE trajectory $\tilde{\kappa}_n$ for the same $p \in \mathbb{N}_0$ which is continuous and passes κ_{n^*} as $n \rightarrow n^*$ along the real axis. Conversely, if κ^* is an IDE such that $J_p(\kappa^*) = 0$, then there locally exists a complex-conjugated pair of complex-valued ITE trajectories $\kappa_n, \bar{\kappa}_n$ as well as a real-valued ITE trajectory $\tilde{\kappa}_n$ all of which are continuous, assigned to the same $p \in \mathbb{N}_0$ and fulfill $\lim_{n \rightarrow n^*} \kappa_n = \lim_{n \rightarrow n^*} \tilde{\kappa}_n = \kappa^*$ for infinitely many $1 \neq n^* > 0$.

Proof. For the first assertion, recall from (8) that

$$\partial_\kappa F_p(n, \kappa) = (n-1)\kappa J_p(\kappa) J_p(\sqrt{n}\kappa), \quad (16)$$

which vanishes at (n^*, κ_{n^*}) according to Corollary 2 with $J_p(\kappa_{n^*}) = J_p(\sqrt{n}\kappa_{n^*}) = 0$ and $J'_p(\kappa_{n^*}) \neq 0 \neq J'_p(\sqrt{n}\kappa_{n^*})$. Hence, the multiplicity of the root $\kappa = \kappa_{n^*}$ within the holomorphic function $\kappa \mapsto F_p(n^*, \kappa)$ is 3. By Hurwitz' theorem we know that the total number of zeros of $\kappa \mapsto F_p(n, \kappa)$, including multiplicity, remains 3 in a small neighborhood of $\kappa = \kappa_{n^*}$ for all n sufficiently close to n^* . Since κ_n is complex-valued for $n \neq n^*$ by assumption and approaches κ_{n^*} as $n \rightarrow n^*$ in complex-conjugated pairs, their combined number of roots is even. Hence, there must be some real-valued trajectory $\tilde{\kappa}_n$ which also goes to κ_{n^*} as $n \rightarrow n^*$. Continuity of $\tilde{\kappa}_n$ in n^* also follows by Hurwitz theorem and elsewhere by the implicit function theorem.

Conversely, let κ^* be an IDE such that $J_p(\kappa^*) = 0$. Then we can find infinitely many $\kappa^{**} \neq \kappa^*$ such that $J_p(\kappa^{**}) = 0$ and set

$$n^* := (\kappa^{**}/\kappa^*)^2 \neq 1. \quad (17)$$

By the same reasoning as above, the total number of roots of $\kappa \mapsto F_p(n^*, \kappa)$ including multiplicity remains 3 in a small neighborhood of κ^* for n sufficiently close to n^* . Thus there exists trajectories $\kappa_{n,1}, \kappa_{n,2}, \kappa_{n,3}$ for $n \in (n^* - \epsilon, n^* + \epsilon)$ for some $\epsilon > 0$ such that $\kappa_{n^*,1} = \kappa_{n^*,2} = \kappa_{n^*,3} = \kappa^*$. These are, in particular, continuous in n^* and differentiable apart of κ^* according to the implicit function theorem. Since $\partial_n F_p(n, \kappa)|_{(n^*, \kappa^*)} \neq 0$ by (9), the 3 trajectories move indeed away from the critical point κ^* . Furthermore, either all 3 of them stay real-valued for $n \neq n^*$ or two of them arise in complex-conjugated pairs. It remains to prove that only the latter can be true: assume contrarily that $\kappa_{n,1}, \kappa_{n,2}, \kappa_{n,3}$ are real-valued trajectories for $n \in (n^* - \epsilon, n^* + \epsilon)$. By Rolle's theorem in case of $\kappa_{n,i} \neq \kappa_{n,j}$ for some $1 \leq i, j \leq 3$ (let then $\kappa_{n,i} < \kappa_{n,j}$ without loss of generality) or by the product rule otherwise, there must be a critical point $\kappa_{n,i,j}$ of the real-analytic function $\kappa \mapsto F_p(n, \kappa)$ for $n \in (n^* - \epsilon, n^* + \epsilon)$ such that

$$\kappa_{n,i} \leq \kappa_{n,i,j} \leq \kappa_{n,j}, \quad (18)$$

in particular $\kappa_{n^*,i,j} = \kappa^*$. Since the roots of J_p are discrete, we get for ϵ sufficiently small that

$$\partial_\kappa F_p(n, \kappa_{n,i,j}) = 0 \quad \Leftrightarrow \quad \kappa_{n,i,j} = \kappa^* \quad \text{or} \quad \kappa_{n,i,j} = \frac{\sqrt{n^*} \kappa^*}{\sqrt{n}}$$

according to (16). In both of the latter cases it holds that $\lim_{n \rightarrow n^*} |\kappa'_{n,i,j}| < \infty$. This contradicts (18) as $n \rightarrow n^*$ since, by the previous lemma, we know that $\lim_{n \rightarrow n^*} \kappa'_{n^*,i} = -\infty$ for all $1 \leq i \leq 3$. \square

Remark 6. *The numerical computation of ITEs which are also IDEs can become rather inaccurate if accompanied by complex-valued ITE trajectories. The reason is that most solution methods also boil down to finding roots of certain residual quantities similar to $\kappa \mapsto F_p(n^*, \kappa)$ which admit in case of non-simple roots a flat, zero-like behavior in a whole neighborhood of the exact root, see [23, p. 106] for example.*

We can also specify the geometric multiplicity of ITEs κ_{n^*} for some $1 \neq n^* > 0$ that are roots of J_p . It is at least 3 for $p = 0$, 5 for $p = 1$ and 6 for $p > 1$ (note a multiplicity of 1 for $p = 0$ and 2 for integer $p > 1$ would be a priori expected according to (2)). The increase originates from additional ITE trajectories $\tilde{\kappa}_n$ with Bessel index $\tilde{p} \in \{p-1, p+1\}$ which passes the IDE as $n \rightarrow n^*$ along the real axis. The latter follows by (5) and $J_{\tilde{p}}(\kappa_{n^*}) \neq 0$, cf. Bourget's hypothesis in [27, p. 484].

Lemma 7. *Let κ_{n^*} be an ITE for some $1 \neq n^* > 0$ such that $J_p(\kappa_{n^*}) = 0$. Then*

$$v_q(r, \varphi) = J_q(\kappa_{n^*}r) \cos(q\varphi), \quad \left(v_q(r, \varphi) = J_q(\kappa_{n^*}r) \sin(q\varphi), q \neq 0 \right),$$

$$w_q(r, \varphi) = \alpha_n \sqrt{n^*} J_q(\sqrt{n} \kappa_{n^*} r) \cos(q\varphi), \quad \left(w_q(r, \varphi) = \alpha_n \sqrt{n^*} J_q(\sqrt{n} \kappa_{n^*} r) \sin(q\varphi), q \neq 0 \right),$$

with $q \in \{p-1, p+1\}$ for $p > 0$ and $q = 1$ for $p = 0$, are linear independent ITP eigenfunction pairs for the ITE κ_{n^*} .

Proof. By Theorem 5 there exists a continuous ITE trajectory κ_n in a neighborhood of n^* which is differentiable for $n \neq n^*$. Consider the limit quotients

$$\begin{aligned} \tilde{v}_q(r, \varphi) &:= \lim_{n \nearrow n^*} \frac{J_p(\kappa_n r) - J_p(\kappa_{n^*} r)}{\kappa_n - \kappa_{n^*}} \cos(q\varphi) = J'_p(r \kappa_{n^*}) r \cos(q\varphi), \\ \tilde{w}_q(r, \varphi) &:= \lim_{n \nearrow n^*} \frac{\alpha_n J_p(\sqrt{n} \kappa_n r) - \alpha_{n^*} J_p(\sqrt{n^*} \kappa_{n^*} r)}{\kappa_n - \kappa_{n^*}} \cos(q\varphi) \\ &= \alpha_{n^*} J'_p(r \sqrt{n^*} \kappa_{n^*}) r \sqrt{n^*} \cos(q\varphi) \\ &\quad + \lim_{n \nearrow n^*} \left(\alpha_n J'_p(r \sqrt{n} \kappa_n) r \frac{\kappa_n}{2\sqrt{n} \kappa'_n} + \frac{\alpha'_n}{\kappa'_n} J_p(r \sqrt{n} \kappa_n) \right) \cos(q\varphi), \end{aligned}$$

whose right-hand sides are obtained by l'Hospital's rule. Here, α'_n denotes the derivative of

$$\alpha_n = \frac{J'_p(\kappa_n)}{\sqrt{n} J'_p(\sqrt{n} \kappa_n)}. \quad (19)$$

This representation is indeed well-defined in a neighborhood of n^* since the roots of J_p and J'_p are distinct and $J_p(\kappa_{n^*}) = 0$ by assumption. We thus obtain

$$\begin{aligned} \alpha'_n &= \frac{J''_p(\kappa_n) \kappa'_n \sqrt{n} J'_p(\sqrt{n} \kappa_n) - J'_p(\kappa_n) \left[\frac{1}{2\sqrt{n}} J'_p(\sqrt{n} \kappa_n) + \sqrt{n} J''_p(\sqrt{n} \kappa_n) \left(\frac{\kappa_n}{2\sqrt{n}} + \sqrt{n} \kappa'_n \right) \right]}{n J'_p(\sqrt{n} \kappa_n)^2} \\ &= (n-1) J'_p(\kappa_n) J_p(\sqrt{n} \kappa_n) \kappa'_n, \end{aligned}$$

where we replaced the second-order derivatives of J_p above via (3). It follows from $\lim_{n \rightarrow n^*} |\kappa'_n| = \infty$ by Lemma 3 that

$$\lim_{n \nearrow n^*} \alpha_n J'_p(r \sqrt{n} \kappa_n) r \frac{\kappa_n}{2\sqrt{n} \kappa'_n} + \frac{\alpha'_n}{\kappa'_n} J_p(r \sqrt{n} \kappa_n) = 0$$

within the definition of $\tilde{w}_q(r, \varphi)$. Thus, we have that both the Dirichlet data of \tilde{v}_q and \tilde{w}_q coincide as well as their Neumann data. The same also holds for

$$\begin{aligned}\widehat{v}_q(r, \varphi) &:= \frac{2p}{r\kappa_{n^*}} J_p(r\kappa_{n^*}) \cos(q\varphi) , \\ \widehat{w}_q(r, \varphi) &:= \alpha_{n^*} \sqrt{n^*} \frac{2p}{r\sqrt{n^*}\kappa_{n^*}} J_p(r\sqrt{n^*}\kappa_{n^*}) \cos(q\varphi) .\end{aligned}$$

However, neither $(\tilde{v}_q, \tilde{w}_q)$ nor $(\widehat{v}_q, \widehat{w}_q)$ satisfy the PDE conditions of (1). Instead, adding or subtracting the recurrence relations

$$2J'_p(x) = J_{p-1}(x) - J_{p+1}(x) \quad \text{and} \quad \frac{2p}{x} J_p(x) = J_{p-1}(x) + J_{p+1}(x) .$$

from each other, respectively, we find that

$$\begin{aligned}v_{p+1}(r, \varphi) &:= \frac{\widehat{v}_{p+1}(r, \varphi) - \tilde{v}_{p+1}(r, \varphi)}{2} = J_{p+1}(\kappa_{n^*}r) \cos((p+1)\varphi) , \\ w_{p+1}(r, \varphi) &:= \frac{\widehat{w}_{p+1}(r, \varphi) - \tilde{w}_{p+1}(r, \varphi)}{2} = \alpha_{n^*} \sqrt{n^*} J_{p+1}(\sqrt{n^*}\kappa_{n^*}r) \cos((p+1)\varphi)\end{aligned}$$

and

$$\begin{aligned}v_{p-1}(r, \varphi) &:= \frac{\widehat{v}_{p-1}(r, \varphi) + \tilde{v}_{p-1}(r, \varphi)}{2} = J_{p-1}(\kappa_{n^*}r) \cos((p-1)\varphi) , \\ w_{p-1}(r, \varphi) &:= \frac{\widehat{w}_{p-1}(r, \varphi) + \tilde{w}_{p-1}(r, \varphi)}{2} = \alpha_{n^*} \sqrt{n^*} J_{p-1}(\sqrt{n^*}\kappa_{n^*}r) \cos((p-1)\varphi)\end{aligned}$$

are linear independent ITP eigenfunction pairs for the ITE κ_{n^*} as long as $p \neq 0$. If $p = 0$, we effectively generate only one additional ITE eigenfunction pair in this way since $J_{-1}(x) = -J_1(x)$ for all x . We can still repeat the proof with sine in place of cosine as angular part, provided $q \neq 0$ and which therefore only affects the case $p = 1$. \square

We finally prove a result for the limiting behavior of complex-valued trajectories as $n \rightarrow \infty$.

Theorem 8. *Let κ_n be a continuous ITE trajectory whose eigenfunction pair (v_n, w_n) is given by (2) for some $p \in \mathbb{N}_0$. Assume that $\kappa_n = \kappa^*$ for infinitely many $n > 1$, where $J_p(\kappa^*) = 0$, and that $y_- \leq \Re(\kappa_n) \leq y_+$ as well as $-C \leq \Im(\kappa_n) \leq C$ for all $n > 1$. Here, $C > 0$ and $y_- < y_+$ are two κ^* -interlacing values that are larger/smaller than the next nearest root of J_p , respectively. Then it holds that $\lim_{n \rightarrow \infty} \kappa_n = \kappa^*$.*

Proof. Assume contrarily that there is a sequence $n_k \rightarrow \infty$ such that either (note that complex-valued ITE trajectories arise in conjugated pairs)

$$\Im(\kappa_{n_k}) > c > 0$$

or that

$$|\Re(\kappa_{n_k}) - \kappa^*| > c > 0$$

for all $k \in \mathbb{N}$ and some $c > 0$. We only present a contradiction to the first inequality under the given assumptions since the second follows by a similar reasoning. Without loss of generality we can even assume, without relabeling, that the k are chosen such that n_k are local maxima of $n \mapsto \Im(\kappa_n)$. Since κ_n is differentiable at n_k by the implicit function theorem, we conclude that

$$\kappa'_{n_k} \in \mathbb{R} \quad (20)$$

for all $k \in \mathbb{N}$. Comparing with the expression of κ'_n in (10), however, we see with $\Im(\kappa_{n_k}) > c$ and the boundedness of κ_n by assumption that

$$\Im\left(\frac{n_k \kappa_{n_k}^2 - p^2}{2n_k(n_k - 1)\kappa_{n_k}}\right) > \Im\left(\frac{\kappa_{n_k} J'_p(\kappa_{n_k})^2}{2n_k(n_k - 1)J_p(\kappa_{n_k})^2}\right)$$

for k sufficiently large due to the different powers of n_k involved on both sides of the inequality. This yields $\Im(\kappa'_{n_k}) \neq 0$ for corresponding k which is a contradiction to (20). \square

Remark 9. *All our findings for the unit disk directly extend to the unit ball in 3D. This follows from the fact that the Fourier Bessel ansatz (2) in 2D just needs to be replaced by*

$$\begin{aligned} v_n(r, \varphi, \theta) &= j_p(\kappa_n r) \cos(p\varphi) P_p^\ell(\cos(\theta)) , \\ (v_n(r, \varphi, \theta) &= j_p(\kappa_n r) \sin(p\varphi) P_p^\ell(\cos(\theta)) , p \neq 0) \end{aligned}$$

and

$$\begin{aligned} w_n(r, \varphi, \theta) &= \alpha_n j_p(\sqrt{n} \kappa_n r) \cos(p\varphi) P_p^\ell(\cos(\theta)) , \\ (w_n(r, \varphi, \theta) &= \alpha_n j_p(\sqrt{n} \kappa_n r) \sin(p\varphi) P_p^\ell(\cos(\theta)) , p \neq 0) , \end{aligned}$$

where $p \in \mathbb{N}_0$ and $\ell \in \{-p, \dots, p\}$. Here, P_p^ℓ is the associated Legendre polynomial and $j_p(x) = \sqrt{\frac{\pi}{2x}} J_{p+\frac{1}{2}}(x)$ is the spherical Bessel function of the first kind of order p satisfying the second-order ordinary differential equation

$$x^2 j_p''(x) + 2x j_p'(x) + (x^2 - p(p+1)) = 0 .$$

The latter is structurally similar to (3) so that corresponding proofs of this section only require minor adaptations. Finally, (4) also becomes

$$f_p(\kappa, n) := \kappa j_p'(\kappa) j_p(\kappa \sqrt{n}) - \kappa \sqrt{n} j_p(\kappa) j_p'(\kappa \sqrt{n}) . \quad (21)$$

3. Numerical Results

In this section, we first present numerical results for the unit disk to visualize our theoretical findings, but to also illustrate novel observations. We will distinguish between the case $n > 1$ and $0 < n < 1$ since they are structurally different. Afterwards, we numerically examine the unit ball in 3D and some standard scattering shapes which will show similar characteristics to the unit disk and therefore inspire a conjecture for more general scatterers.

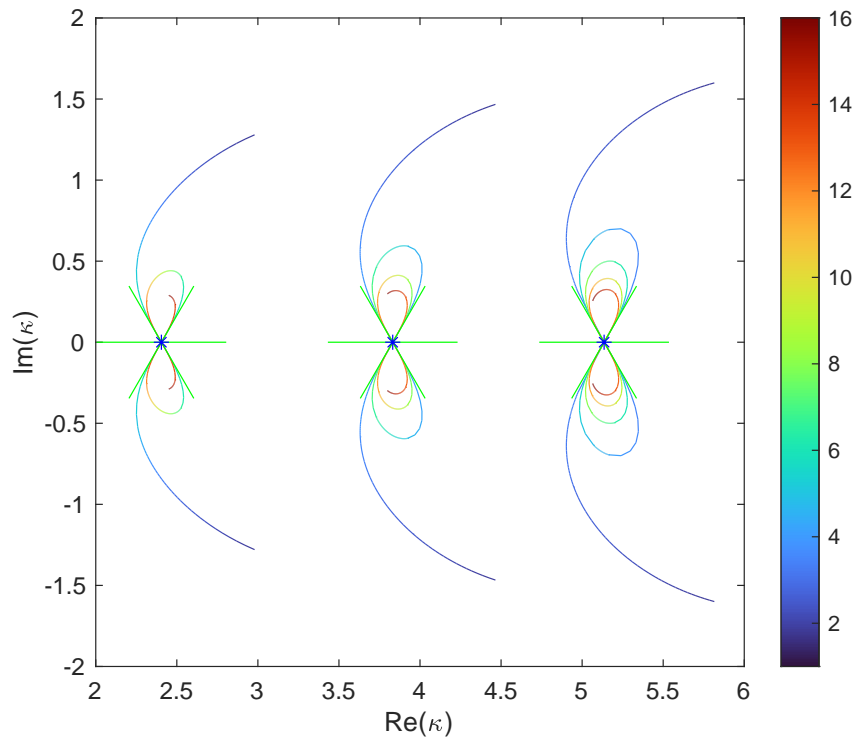


Figure 1. The first three complex-conjugated pairs of complex-valued ITE trajectories for the unit disk and $p \in \{0, 1, 2\}$, respectively, using $n \in (1, 16]$.

3.1. The unit disk for $n > 1$

The first complex-valued roots κ_n of the function F_p from (4) (ordered by real parts) are computed for $p \in \{0, 1, 2\}$ and sufficiently many $n \in (1, 16]$ via Beyn's second integral algorithm, see [2, p. 3860]. Using interpolation with respect to n to obtain smooth curves, Figure 1 shows the resulting output where the color bar refers to the varying index of refraction $n > 1$.

As we observe, the trajectories come in complex-conjugated pairs and arise at certain points satisfying $\text{Im}(\kappa_n) \neq 0$ for n close to one. For increasing n they reapproach the first three IDEs of the unit disk which are marked by blue asterisks in Figure 1 and are approximately given by 2.4048, 3.8317, and 5.1356, respectively, see [1]. For instance, the first complex-conjugated trajectories pair corresponds to $p = 0$ and passes through 2.4048 for the first time at $n \approx 5.2689$ and then for $n \approx 12.9491$. These n coincide, in agreement with (17), with the squared ratio of successive larger roots than 2.4048 of J_0 and 2.4048 itself, respectively. In particular, the ambiguity of (17) is reflected by recurrence of the complex-valued ITE trajectories towards the same IDE. Also note that incident and outgoing angles at IDEs are restricted to $\pm\pi/3$ as predicted by Lemma 3 which is highlighted additionally in the figure by green lines. Further, the trajectory pair tends to converge as a whole towards 2.4048 for growing n , cf. Theorem 8. The other two complex-conjugated trajectory pairs in Figure 1 corresponding to $p = 1$ and

$p = 2$ behave likewise and are not discussed in further detail.

Most notably, we could not find any other ITE trajectories than the IDE-recurrent ones in the complex plane. Also, within our numerical experiments every IDE has been linked to exactly one complex-conjugated pair of recurrent and apparently convergent trajectories. These observations have also been made for larger Bessel indices $p > 2$ or larger IDEs. Hence, there seems to be a one-to-one correspondence between IDEs and complex-valued ITE trajectories.

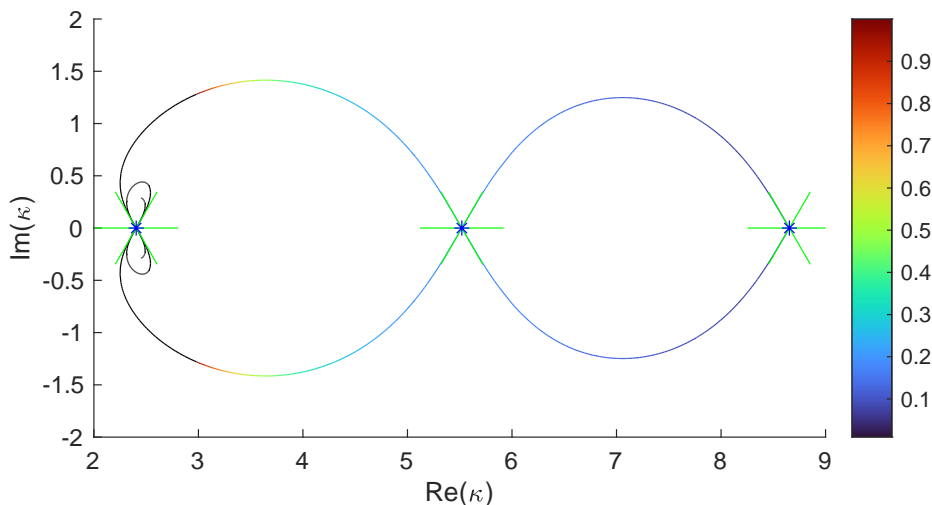


Figure 2. The first complex-conjugated pair of complex-valued ITE trajectories for the unit disk and $p = 0$ from Figure 1 extended to $n \in (0, 16]$ (color bar refers to $n < 1$ only).

3.2. The unit disk for $0 < n < 1$

In Figure 2, we plot for $p = 0$ and the first complex-conjugated pair of complex-valued ITE trajectories of the unit disk from the previous subsection the trajectory continuation in $0 < n < 1$. We observe that it connects continuously through $n = 1$ – for which the ITP is formally not defined – to $n > 1$ (shown here in black for $n \in (1, 16]$ and copied from Figure 1). As before, we used Beyn’s second integral algorithm to generate the trajectories.

We directly notice that the eigenvalue trajectories for $0 < n < 1$ behave different from the ones for $n > 1$. Indeed, for $0 < n < 1$ the trajectories are not recurrent any more but escape to infinity as $n \rightarrow 0$, crossing the real axis at successive IDEs instead.

For instance, the second IDE 5.5201 is hit for $n \approx 0.1898$ and the third IDE 8.6537 for $n \approx 0.0772$ which can again be verified by evaluating (17) correspondingly. Also note that ingoing and outgoing directions at IDEs are now given by $\pm 2\pi/3$, cf. Lemma 3. Since $\kappa_n = \kappa_{1/n}/\sqrt{n}$ for any $n > 1$ by symmetry of the ITP, it suffices to confine ourselves to the case $n > 1$ in the sequel.

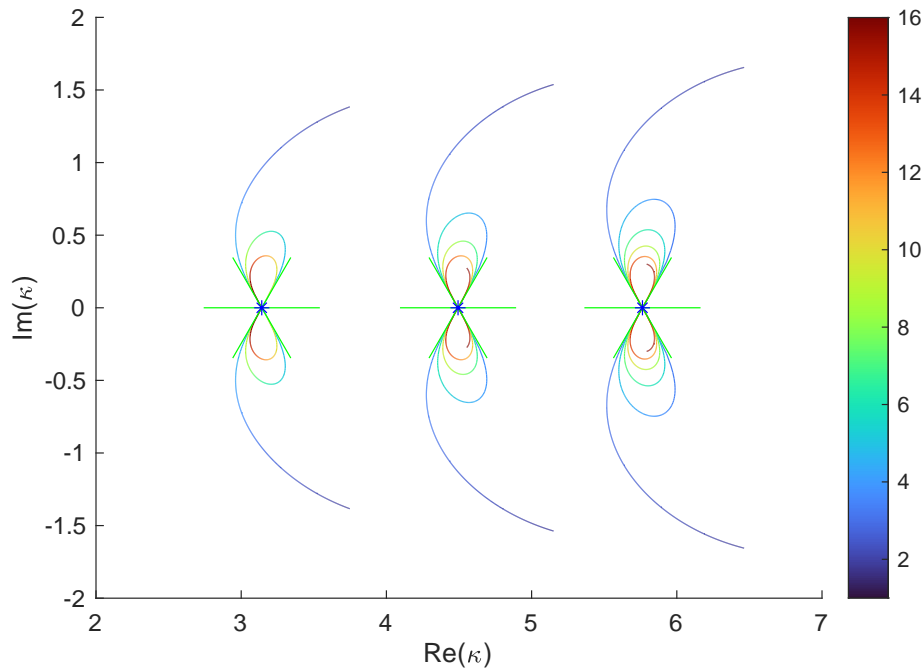


Figure 3. The first three complex-conjugated pairs of complex-valued ITE trajectories for the unit ball and $p \in \{0, 1, 2\}$, respectively, using $n \in (1, 16]$.

3.3. The unit ball for $n > 1$

In Figure 3, we provide a 3D example with the first three complex-conjugated pairs of complex-valued ITE curves for the unit ball using $n \in (1, 16]$ and $p \in \{0, 1, 2\}$, cf. Remark 9. For this purpose, we need to compute the complex-valued roots of (21) instead of (4) and can then proceed as in Figure 1.

We recognize a similar behavior as for the unit disk. Specifically for $p = 0$, which is the case of spherically symmetric ITP eigenfunctions, Colton & Leung already pointed out in [9] that ITEs can only be real-valued for $n = q^2$ or $n = 1/q^2$, where $q \in \mathbb{N}$. From our perspective of ITE trajectories, this implies that there are simultaneous intersections with infinitely many IDEs for the same n . This can be seen from $j_0(\kappa) = \sin(\kappa)/\kappa$ which has equidistant roots (and thus IDEs) at $\kappa^* \in \mathbb{N}\pi$. Comparing with (17) yields $n^* = (qm\pi)^2/(m\pi)^2 = q^2$ for any $m \in \mathbb{N}$, that is, complex-valued ITE trajectories

intersect $\kappa^* = m\pi$ for all $m \in \mathbb{N}$ simultaneously whenever $n = q^2$, $q \in \mathbb{N}$. Such a simultaneous recurrence has not been observed for the unit disk. Note here that roots of J_0 as well as of higher order Bessel functions are only asymptotically equidistant, see [1, 4].

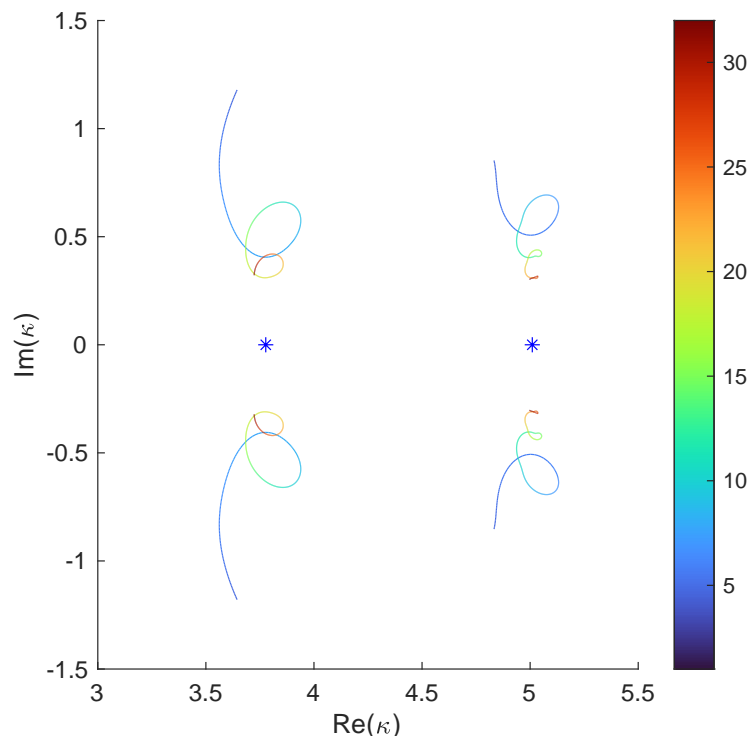


Figure 4. The first two complex-conjugated pairs of complex-valued ITE trajectories for the ellipse with semi-axis 1 and 0.5 using $n \in [4, 32]$.

3.4. The ellipse for $n > 1$

Next, we consider an ellipse with semi-axis 1 and $b = 0.5$ which can be regarded as a small perturbation of the unit disk. Since a separation of variable ansatz does not simplify to a decoupled analytical expression as in (4), we employ the modified method of fundamental solution (modified MFS) to compute approximate ITEs, see [19, Section 3.2] for more details on this algorithm. In its original notation, we placed $m_I = 10$ nodes on a circle with radius $0.8 \cdot b$ inside the ellipse, $m = 40$ collocation points along the ellipse's boundary and $m = 40$ source points on an exterior circle with radius 4. When referring to the modified MFS in the remainder of this section, we assume that all the auxiliary circles have the same center as the scattering object itself. Further, since ITEs are computed within the modified MFS as minimizers of some boundary collocation misfit function, we always take the computed ITE from the previous n as initial guess when incrementing n . Thus we are only left to set one independent initial guess for the complex-valued ITE at the minimal n of interest which we will fix as $n = 4$.

For the ellipse with semi-axis 1 and $b = 0.5$, we picked $4 \pm i$ and $5 \pm i$ as independent initial guesses to compute the first two complex-conjugated pairs of complex-valued ITE trajectories, respectively. The resulting curves for $n \in [4, 32]$ are shown in Figure 4. Unlike for the disk or the ball, however, the ITE trajectories are not recurrent with respect to IDEs any more, which were computed approximately as 3.777 and 5.010 according to the formula given in [13, pp. 9]. Instead, they tend to spiral down towards a unique IDE without touching the real axis at all. We therefore still observe a one-to-one correspondence between IDEs and complex-valued ITE trajectories which is now more generally governed by the limiting behavior of the latter as $n \rightarrow \infty$.

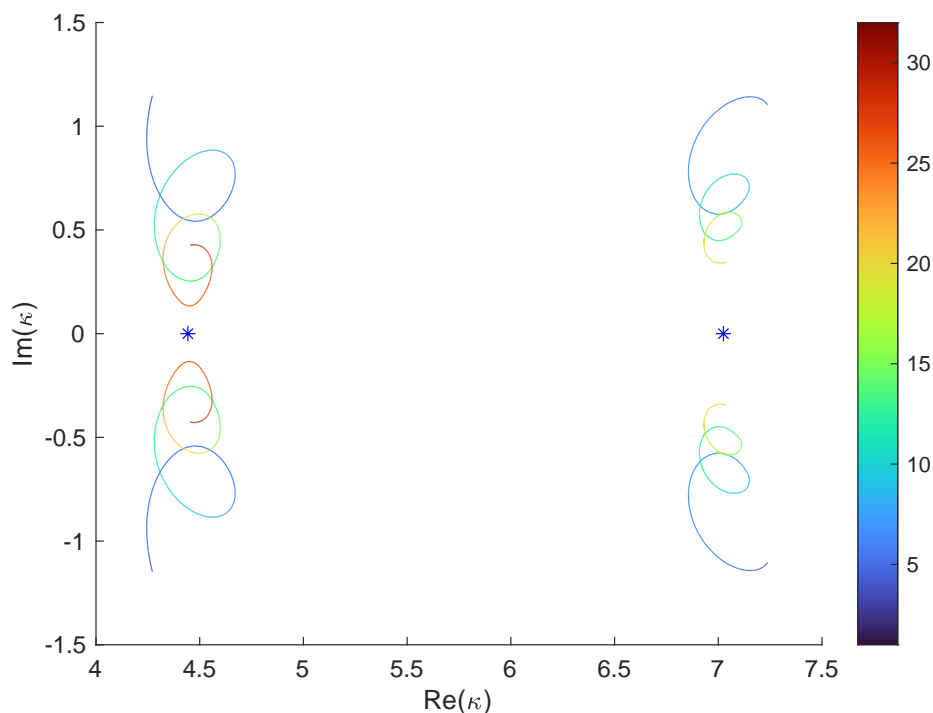


Figure 5. The first two complex-conjugated pairs of complex-valued ITE trajectories for the unit square using $n \in [4, 32]$ and $n \in [4, 20]$, respectively.

3.5. The unit square for $n > 1$

In order to also include more disk-unrelated scatterers into our scope of investigation, we turn our attention now to the unit square as an example with a non-smooth boundary. Here, the modified MFS has been exploited with $m_I = 20$ nodes on an interior circle with radius 0.25, $m = 61$ collocation points along the boundary of the square apart from its corners (as the outer normal ν would not be defined otherwise) and $m = 61$ source points on an exterior circle with radius 0.75. The first two complex-conjugated pairs of complex-valued ITE trajectories are displayed in Figure 5, taking $4.5 \pm i$ and $7 \pm i$ as independent initial guesses at $n = 4$, respectively.

In contrast to the ellipse, the two trajectory pairs are now plotted with respect to different yet overlapping parameter domains of n which is $[4, 32]$ for the first and $[4, 20]$ for the second. The reason is that the modified MFS generally suffers from ill-conditioning effects for large wave numbers. In particular, neither κ_n in v_n nor $\sqrt{n}\kappa_n$ in w_n can be too large within (2), so that especially the latter restricts the admissible choices of n . In our plot both resulting trajectory pairs show again a spiral pattern which approach for growing n the separated blue asterisks on the real axis, respectively. They are given by $\sqrt{2}\pi \approx 4.4429$ and $\sqrt{5}\pi \approx 7.0248$ according to the first two IDEs of the unit square in [13, pp. 6]. We still observe a one-to-one correspondence between IDEs and complex-conjugated pairs of complex-valued ITE trajectories similar to the ellipse.

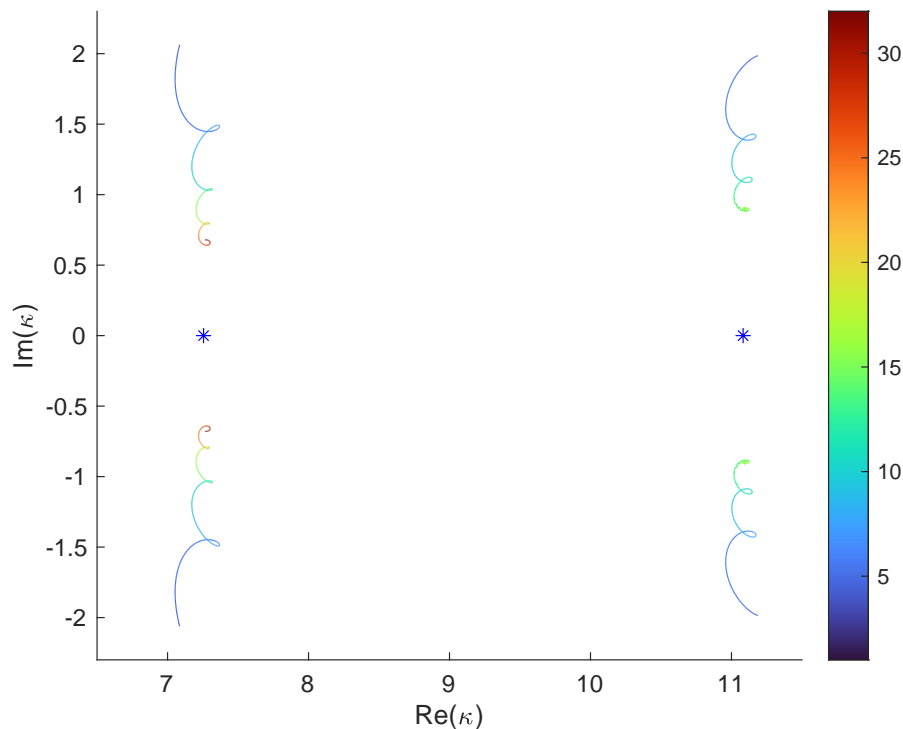


Figure 6. The first two complex-conjugated pairs of complex-valued ITE trajectories for the equilateral triangle with side length one using $n \in [4, 32]$ and $n \in [4, 16]$, respectively.

3.6. The equilateral triangle for $n > 1$

We also consider an equilateral triangle with side length one for which the first two IDEs are given by $4\pi/\sqrt{3} \approx 7.255$ and $4\pi\sqrt{7}/3 \approx 11.082$, see [13, pp. 10–11]). Using the same parameters within the modified MFS as for the unit square but changing $m = 61$ to $m = 51$ for the first trajectory pair yields the two complex-conjugated pairs of complex-valued ITE trajectories shown in Figure 6. The domain of n was $n \in [4, 32]$

for the first pair and $n \in [4, 16]$ for the second. As independent initial ITE guesses at $n = 4$ we took $7.3 \pm 1.5i$ and $11 \pm 2i$, respectively. Altogether, we again observe a one-to-one correspondence between IDEs and complex-conjugated pairs of complex-valued ITE trajectories which tend to approach each other as n gets larger.

3.7. The deformed ellipse

At last, we present an example of a non-convex scatterer which is parametrized for $t \in [0, 2\pi)$ by

$$t \mapsto \begin{pmatrix} 0.75 \cos(t) + 0.3 \cos(2t) \\ \sin(t) \end{pmatrix}. \quad (22)$$

Its exact shape is illustrated in Figure 8. In this case, we employ the modified MFS

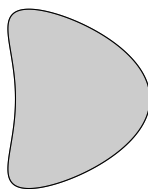


Figure 7. The deformed ellipse parametrized by (22)

both for computing the first two IDEs of the deformed ellipse and for generating the first two pairs of complex conjugated ITE trajectories. Specifically, we distributed $m_I = 20$ nodes on an interior circle with radius 0.2, $m = 51$ collocation points along the boundary of the scatterer and $m = 51$ source points on an exterior circle with radius 1.5. The independent initial guesses were chosen as $3 \pm 0.8i$ and $4 + 0.8i$ for which the corresponding output is shown in Figure 8 within the ranges $n \in [4, 32]$ and $n \in [4, 20]$, respectively. We feel at this point like we have checked enough samples of scatterers all of which admit the same characteristics for IDEs and complex-valued ITE trajectories to finally formulate a more general conjecture below.

Conclusion

We have shown that complex-valued eigenvalue trajectories for the interior transmission problem of the unit disk parametrized by the homogeneous index of refraction intersect the real axis only at interior Dirichlet eigenvalues of the negative Laplacian. The intersections occur at specific angles distinguishing the cases $0 < n < 1$ and $n > 1$. Further, it is shown that IDE-recurrent complex-valued ITE curves are actually convergent as $n \rightarrow \infty$. Numerical results are given for an ellipse, a deformed ellipse, a unit square, and an equilateral triangle which show a similar spiral behavior towards IDEs as n grows. In addition, results are given for a unit sphere for which our provided

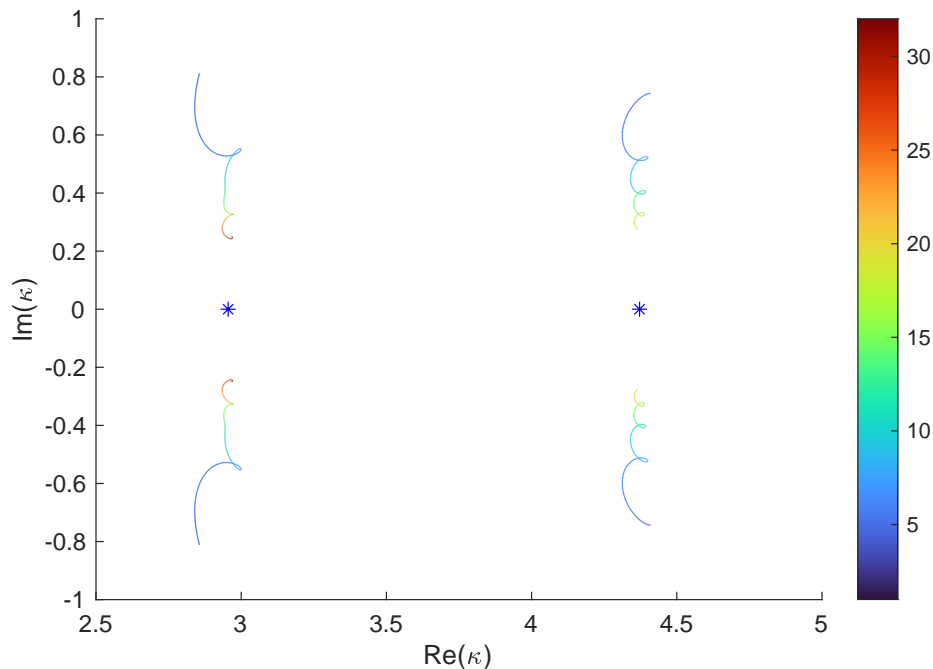


Figure 8. The first two complex-conjugated pairs of complex-valued ITE trajectories for the deformed ellipse from (22) using $n \in [4, 32]$ and $n \in [4, 20]$, respectively.

theory works the same way as for the unit disk. We conclude that there seems to be a one-to-one correspondence between Dirichlet eigenvalues of the Laplacian and complex-valued interior transmission eigenvalue trajectories. We state this finding in a conjecture as follows:

Conjecture 1. *There is a one-to-one correspondence between complex-valued ITE trajectories and IDEs for simply-connected scatterers. More precisely, any complex-valued ITE trajectory κ_n converges to some IDE as $n \rightarrow \infty$. Conversely, for any IDE there exists exactly one complex-conjugated pair of complex-valued ITE trajectories which converges to that IDE as $n \rightarrow \infty$.*

Its further investigation will be subject of future research. From the numerical point of view, we have seen that the modified method of fundamental solution produces inaccurate results for large wave numbers and in particular for large n . Hence, we will investigate on how to circumvent this problem probably through the use of the computationally more demanding boundary element collocation method. Finally, the electromagnetic or elastic interior transmission problem will be investigated as well as a potential generalisation of the current results to inhomogeneous media.

Acknowledgments

Lukas Pieronek was funded by the Deutsche Forschungsgemeinschaft (DFG, German Research Foundation) - SFB 1173.

References

- [1] M. Abramowitz and I. A. Stegun. *Handbook of mathematical functions with formulas, graphs, and mathematical tables*, volume 55. US Government printing office, 1964.
- [2] W.-J. Beyn. An integral method for solving nonlinear eigenvalue problems. *Linear Algebra and its Applications*, 436(10):3839–3863, 2012.
- [3] E. Blåsten, X. Li, H. Liu, and Y. Wang. On vanishing and localizing of transmission eigenfunctions near singular points: a numerical study. *Inverse Problems*, 33(10):105001, 2017.
- [4] S. Breen. Uniform upper and lower bounds on the zeros of Bessel functions of the first kind. *Journal of Mathematical Analysis and Applications*, 196(1):1–17, 1995.
- [5] K. A. Broughan. Holomorphic flows on simply connected regions have no limit cycles. *Meccanica*, 38(6):699–709, 2003.
- [6] F. Cakoni, D. Colton, and D. Gintides. The interior transmission eigenvalue problem. *SIAM Journal on Mathematical Analysis*, 42(6):2912–2921, 2010.
- [7] F. Cakoni and H. Haddar. On the existence of transmission eigenvalues in an inhomogeneous medium. *Applicable Analysis*, 88(4):475–493, 2009.
- [8] D. Colton, A. Kirsch, and L. Päivärinta. Far-field patterns for acoustic waves in an inhomogeneous medium. *SIAM Journal on Mathematical Analysis*, 20(6):1472–1483, 1989.
- [9] D. Colton and Y.-J. Leung. Complex eigenvalues and the inverse spectral problem for transmission eigenvalues. *Inverse Problems*, 29(10):104008, 2013.
- [10] D. Colton, Y.-J. Leung, and S. Meng. Distribution of complex transmission eigenvalues for spherically stratified media. *Inverse problems*, 31(3):035006, 2015.
- [11] H. Geng, X. Ji, J. Sun, and L. Xu. C^0 IP methods for the transmission eigenvalue problem. *Journal of Scientific Computing*, 68(1):326–338, 2016.
- [12] D. Gintides and N. Pallikarakis. A computational method for the inverse transmission eigenvalue problem. *Inverse Problems*, 29(10):104010, 2013.
- [13] D. S. Grebenkov and B.-T. Nguyen. Geometrical structure of Laplacian eigenfunctions. *SIAM Review*, 55(4):601–667, 2013.
- [14] J. Han and Y. Yang. An adaptive finite element method for the transmission eigenvalue problem. *Journal of Scientific Computing*, 69(3):1279–1300, 2016.
- [15] J. Han and Y. Yang. An H^m -conforming spectral element method on multi-dimensional domain and its application to transmission eigenvalues. *Science China Mathematics*, 60(8):1529–1542, 2017.
- [16] J. Han, Y. Yang, and H. Bi. A new multigrid finite element method for the transmission eigenvalue problems. *Applied Mathematics and Computation*, 292:96–106, 2017.
- [17] A. Kirsch. The denseness of the far field patterns for the transmission problem. *IMA Journal of Applied Mathematics*, 37(3):213–225, 1986.
- [18] A. Kleefeld. A numerical method to compute interior transmission eigenvalues. *Inverse Problems*, 29(10):104012, 2013.
- [19] A. Kleefeld and L. Pieronek. The method of fundamental solutions for computing acoustic interior transmission eigenvalues. *Inverse Problems*, 34(3):035007, 2018.
- [20] N. N. Lebedev and R. A. Silverman. *Special functions and their applications*. Courier Corporation, 1972.
- [21] Y.-J. Leung and D. Colton. Complex transmission eigenvalues for spherically stratified media. *Inverse Problems*, 28(7):075005, 2012.

- [22] H. Li and Y. Yang. An adaptive C^0 IPG method for the Helmholtz transmission eigenvalue problem. *Science China Mathematics*, 61(8):1519–1542, 2018.
- [23] L. Pieronek. *The method of fundamental solutions for computing interior transmission eigenvalues*. PhD thesis, BTU Cottbus-Senftenberg, 2020.
- [24] B. P. Rynne and B. D. Sleeman. The interior transmission problem and inverse scattering from inhomogeneous media. *SIAM Journal on Mathematical Analysis*, 22(6):1755–1762, 1991.
- [25] G. Vodev. High-frequency approximation of the interior Dirichlet-to-Neumann map and applications to the transmission eigenvalues. *Analysis & PDE*, 11(1):213–236, 2017.
- [26] S. Wang, H. Bi, Y. Zhang, and Y. Yang. A two-grid discretization scheme of non-conforming finite elements for transmission eigenvalues. *Computers & Mathematics with Applications*, 75(2):520–533, 2018.
- [27] G. N. Watson. *A treatise on the theory of Bessel functions*. Cambridge University Press, 1995.
- [28] Y. Xi and X. Ji. Recursive integral method for the nonlinear non-selfadjoint transmission eigenvalue problem. *Journal of Computational Mathematics*, 35(6):828–838, 2017.
- [29] Y. Xi, X. Ji, and S. Zhang. A multi-level mixed element scheme of the two-dimensional Helmholtz transmission eigenvalue problem. *IMA Journal of Numerical Analysis*, 40(1):686–707, 2018.
- [30] Y. Yang, H. Bi, H. Li, and J. Han. Mixed methods for the Helmholtz transmission eigenvalues. *SIAM Journal on Scientific Computing*, 38(3):A1383–A1403, 2016.
- [31] Y. Yang, H. Bi, H. Li, and J. Han. A C^0 IPG method and its error estimates for the Helmholtz transmission eigenvalue problem. *Journal of Computational and Applied Mathematics*, 326:71–86, 2017.
- [32] Y. Yang, J. Han, and H. Bi. Non-conforming finite element methods for transmission eigenvalue problem. *Computer Methods in Applied Mechanics and Engineering*, 307:144–163, 2016.